Dynamic response of clamped sandwich beams with fluid-fillied corrugated cores

Xin Wang[a,c], Run-Pei Yu[a,c], Qian-Cheng Zhang[a,d,*], Lang Li[a,c], Xue Li[b,c], Zhen-Yu Zhao[b,c], Bin Han[e], Si-Yuan He[f], Tian Jian Lu[b,c,*]

[a] State Key Laboratory for Strength and Vibration of Mechanical Structures, Xi'an Jiaotong University, Xi'an 710049, PR China
[b] State Key Laboratory of Mechanics and Control of Mechanical Structures, Nanjing University of Aeronautics and Astronautics, Nanjing 210016, PR China
[c] Nanjing Center for Multifunctional Lightweight Materials and Structures (MLMS), Nanjing University of Aeronautics and Astronautics, Nanjing 210016, PR China
[d] Key Laboratory of Intense Dynamic Loading and Effect, Northwest Instituteof Nuclear Technology, Xi'an, 710024, China
[e] School of Mechanical Engineering, Xi'an Jiaotong University, Xi'an 710049, PR China
[f] School of Biological Science & Medical Engineering, Southeast University, Nanjing 210016, PR China

ARTICLE INFO

ABSTRACT

The effect of fluid filling on the dynamic response of corrugated sandwich beams under simulated blast loading with close-celled metallic foam projectile was systematically investigated. Deformation and failure modes as well as displacement/contact force/energy absorption histories of water-filled sandwich beams were obtained at different impact levels and compared with those of empty sandwich beams. Subsequently, a combined smoothed particle hydrodynamics-finite element (SPH-FE) model was employed to simulate the dynamic responses of water-filled sandwich beams, explore the underlying mechanisms, and assess the influence of fluid-filling and sealing material on permanent beam deflection. Good agreement was achieved between numerical simulations and experimental measurements. Under impact loading, the filled liquid provides strong interaction between fluid and sandwich components owing to its inertia and incompressibility. Fluid-filling led to not only significantly reduced permanent deflection of both face sheets but also considerably enhanced resistance of the corrugated core against plastic buckling and progressive folding

1. Introduction

Lightweight sandwich structures composed of thin, stiff, strong face sheets and low-density cellular cores typically exhibit superior blast/ impact resistance relative to equivalent monolithic counterparts, mainly for the following mechanisms [1]: (i) smaller transferred momentum as a result of fluid-structure interaction (FSI), especially for underwater blast; (ii) sufficient plastic collapse and excellent energy absorption of cellular core; (iii) increased bending strength of sandwich construction. In recent years, a multitude of sandwich structures subjected to different types of impulsive loading (*e.g.*, air blast [2], underwater blast [3], local projectile impact [4]) are systematically investigated, with particular focus placed upon exploring their dynamic deformation and failure mechanisms. Consequently, with ever increasing requirement of blast/impact resistance, it has been envisioned that well-designed sandwich constructions are attractive candidates for replacing traditional monolithic plates or beams in engineering applications, such as ship hulls [5] and armored vehicle underbodies [6].

Nevertheless, in heavily loaded structures, sandwich structures must be used with caution for large structural deformation may result in stress concentration at the attachment points between the face sheets and cores, causing thus catastrophic failure at lower intensity impulse levels compared with monolithic plates [4,7]. Thus, in order to maintain structural integrity over a wide intensity range of impulsive loading, there is a longstanding need to explore effective approaches for further enhancing the blast/impact resistance of sandwich structures.

Recently, a burgeoning interest is growing on adopting the concept of hybrid design to strengthen the mechanical properties of sandwich structures having cellular cores [8,9], including compression/bending/ shear stiffness and strength [10–12], modal characteristics [13] and blast/impact resistance [14]. Typically, one or more advanced materials are inserted or in-situ synthesized in the abundant space of cellular cores to construct hybrid sandwich cores. The most widely-used fillers are high-porosity cellular materials (e.g., honeycombs and polymer/ metallic foams), for these cellular materials can not only enhance the energy absorption capacity of the sandwich core but also improve the
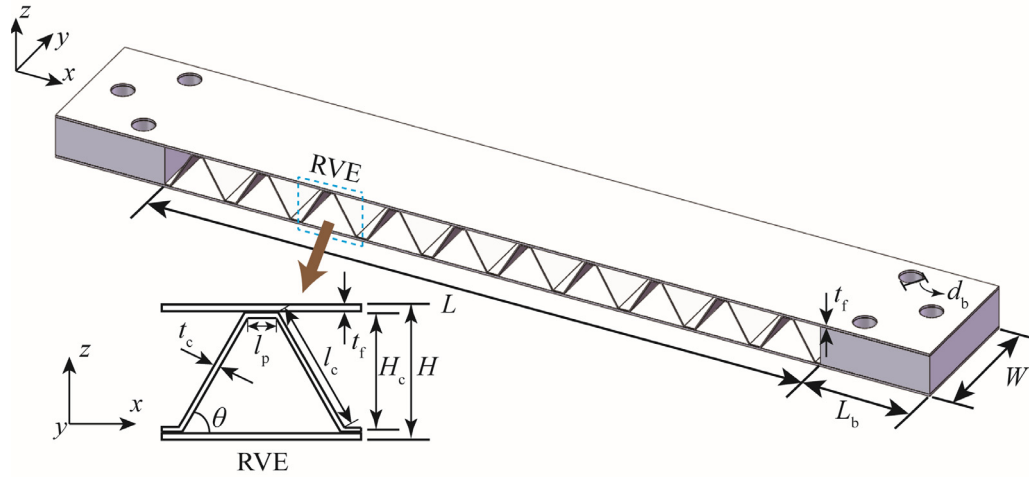

Fig. 1. Geometric configuration of sandwich beam with corrugated core.

bending stiffness/strength of the whole structure. For typical example, Lu and his colleagues [15–17] systematically studied the blast and ballistic penetration performance of hybrid-cored sandwich structures with close-celled aluminum foam used as the filler, and further revealed the underlying deformation and failure mechanisms. Then, a series of efforts by Zhang et al. [18,19] and Yazici et al. [20,21] demonstrated the substantial beneficial effects of foam filling on resisting structural deformation under air blast loading or shock tube impulse. Built upon similar mechanisms, a widely used energy-absorbing component, the thin-walled circular tube, was inserted into honeycomb cores to construct hybrid-cored sandwiches, with excellent blast resistance achieved by tailoring the filling configuration [22,23]. Meanwhile, to satisfy severe requirements of specific engineering applications, like removable shelters and fortifications against terrorism, the filling strategy should be properly designed to possess such features as high availability, simple fabrication and quick mounting. To this end, Børvik et al. [24,25] proposed to use granular materials (*e.g.*, sand, gravel, crushed stone and crushed rock) as the filler to improve the blast and penetration resistance of corrugated-core protective structures. Compared with cellular foams, the granular materials provide much stronger interaction against core member buckling and plastic bending, and significantly improve the overall inertia. At present, hybrid-cored sandwich designs focused mainly upon choosing solid fillers with certain degree of compressibility, and little attention is paid to using fluid like bulk water as the filler for hybrid sandwich construction.

Over the past decades, the effects of water (e.g., bulk water, water mist) on attenuating blast shock wave have been extensively studied [26], with excellent reduction in peak pressure and impulse achieved, especially when the water is stored close to the explosive [27–29]. The underlying mechanisms mainly include: (i) momentum transfer, that means the impulse induced by the explosive is partly transferred to the kinematic acceleration of the bulk water; (ii) latent heat absorption by evaporation of the bulk water; (iii) quenching of secondary reactions by the water mist [28]. In addition, the bulk water stored in a confined structure (e.g., tank [30,31], tube [32–34], cabin [35]) can help to reduce blast/impact-induced deformation via the FSI effect, owing to its inertia and incompressibility. It is interesting therefore to evaluate how the performance of lightweight sandwich structures with cellular cores under blast loading can be improved by filling bulk water into the core, and explore the corresponding mechanisms.

Experimentally, foam projectile impacting, instead of high-risk explosives, has been extensively employed at the laboratory scale to preliminarily assess the dynamic performance of all-metallic or composite sandwich structures [36–38], which was firstly presented by Radford et al. [39]. The impact impulse transferred to the targets can be expressed as:

$$I_p = \rho_p l_0 v_0 \qquad (1)$$

where ρ_p, l_0, σ_p and ε_D is the density, length, plateau strength and densification strain of the foam projectile (e.g., close-celled aluminum foam), respectively, and v_0 is the impact velocity. Therefore, different impact impulses can be realized through appropriate selection of foam density and velocity and hence may be employed, to a good approximation, to replace the blast impulse loading of an explosive charge in the present tests.

The main objective of the current study was to provide comprehensive understanding of: (i) the effects of liquid filling on local impact resistance of corrugated sandwich beams, including deformation/failure modes, permanent deflection of face sheets, core compression, and the onset of failure, (ii) the accuracy of full finite element simulations in predicting the dynamic structural response of liquid-filled sandwich beams, (iii) the dependence of structural deformation on the mechanical and physical properties of the filled fluid and the sealing material. This paper was organized as follows. Section 2 presented details concerning the fabrication and sealing procedures of corrugated sandwich beams. Section 3 provided a comprehensive experimental comparison of both empty and water-filled sandwich beams under different foam projectile impact, and the benefits of water filling on resisting impact-induced deformation were analyzed. In Section 4, both finite element (FE) model and combined smoothed particle hydrodynamics-finite element (SPH-FE) model were introduced, validated and further employed to predict the dynamic structural response of water-filled sandwich beams and explore the underlying mechanisms.

2. Experimental methodology

Fig. 1 displayed the geometry and representative volume element (RVE) of end-clamped, all-metallic sandwich beam with corrugated core. Relevant geometric parameters were: length L, width W and total thickness H of sandwich beam; face sheet thickness t_f; core height H_c; thickness t_c, length l_c and inclination angle θ of corrugation member; corrugation platform length l_p; metal block length L_b; and bolt hole diameter d_b. The relative density of the corrugated core, $\bar{\rho}$, could be expressed as:

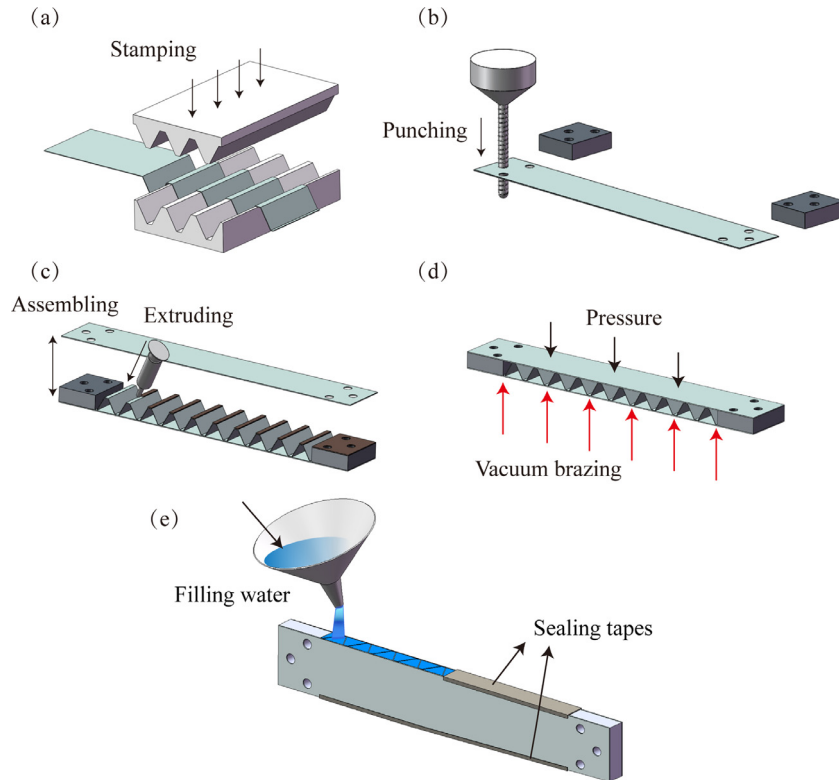$$\bar{\rho} = \frac{t_c(l_p + l_c)}{(l_p + l_c \cos\theta)(t_c + l_c \sin\theta)} \qquad (2)$$

Fig. 2. Fabrication process of corrugated sandwich beam: (a) stamping, (b) punching, (c) assembling, (d) vacuum brazing, and (e) sealing.

2.1. Fabrication process

Sandwich beam samples were made from AISI 304 stainless steel, and comprised of two identical face sheets and either empty or water-filled corrugated cores. As shown in Fig. 2, the fabrication process was summarized into four main steps: (i) forming corrugated core via stamping, (ii) punching the face sheets and the metal blocks (for end-clamping), (iii) assembling the face sheets, the corrugated core and the metal blocks, and (iv) vacuum brazing in furnace. Note that, for end clamping, three holes of diameter $d_b = 10$ mm on each side of the sandwich beam were milling-machined on both the face sheets and metal blocks. To achieve a fully clamped boundary condition, the metal blocks were inserted to get a full-densification of sandwich core between the fixtures under impact loading. Vacuum brazing was conducted with BNi-7 braze alloy at the brazing temperature of 1040℃, and held for 15 min at vacuum atmosphere of 5×10^{-3} Pa to let capillarity draw the braze alloy into the joints. The chemical composition of BNi-7 brazing alloy was listed in Table 1, while detailed geometric parameters of as-brazed test samples were summarized in Table 2. Additional fabrication procedures considered in the current study were: (i) for improved bonding between the corrugated core and face sheets, a corrugation platform was reserved [7]; (ii) given the loss of brazing joints, the thickness t_c of the corrugation member was selected to be larger than 0.2 mm to ensure node integrity [40].

The corrugated core was filled with bulk water of density $\rho_w = 1000$ kg m^{-3} and dynamic viscosity $\eta_w = 8.9 \times 10^{-4}$ Pa s and then sealed using rubberized waterproof tape [41] (Fig. 2e). The thickness and density of the sealing tape were measured as 0.7 mm and

Table 1
Chemical composition of BNi-7 brazing alloy (unit: wt.%).

Ni	Cr	Si	Fe	B	P	C	S	Solidus	Brazing temperature
Bal.	14	0.1	0.2	0.02	10.1	0.06	0.02	888℃	927~1093℃

Table 2
Geometric parameters of as-brazed sandwich samples (unit: mm).

L	W	t_f	l_c	l_p	t_c	θ	L_b	d_b	$\bar{\rho}$
300	60	1	20	5	0.5	60°	40	10	4.68%

1174 kg m^{-3}, respectively.

2.2. Material characterization

While the face sheets and corrugated cores of the sandwich beams were both manufactured from AISI 304 stainless steel (Haocheng Co., Ltd, Shanghai), close-celled aluminum foam projectiles were fabricated by a melt foaming process using 1.2 wt.% TiH$_2$ as the foaming agent at 675℃. The rubberized waterproof sealing tape (Flex Tape®, USA) was used as the sealing material (Fig. 2), and the milky sealant (Teroson MS939, Henkel) was used to cover small gaps around the sealing material to avoid leakage.

Quasi-static uniaxial compressive test of the present close-celled aluminum foam (density $\rho_p = 378.3$ kg m^{-3}) was conducted at a nominal strain rate of 1×10^{-3} s^{-1}, using cylindrical foam specimens of diameter 25 mm and height 50 mm [42]. Fig. 3a presented the measured stress versus strain curve, from which the plateau strength of the aluminum foam was obtained as $\sigma_p = 4.1$ MPa. To identify the nominal densification strain ε_D of the foam, the energy efficiency parameter χ was defined, as follows [43]:
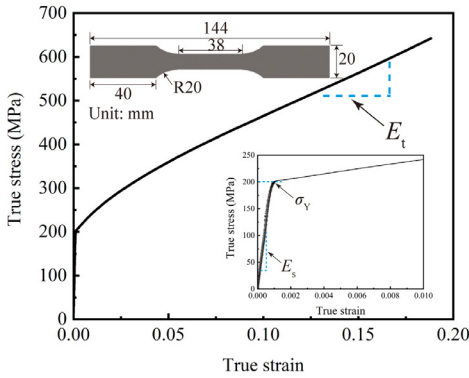
$$\chi(\varepsilon) = \frac{1}{\sigma(\varepsilon)} \int_0^\varepsilon \sigma(\varepsilon) d\varepsilon \tag{3}$$

$$\left. \frac{d\chi(\varepsilon)}{d\varepsilon} \right|_{\varepsilon=\varepsilon_D} = 0 \tag{4}$$
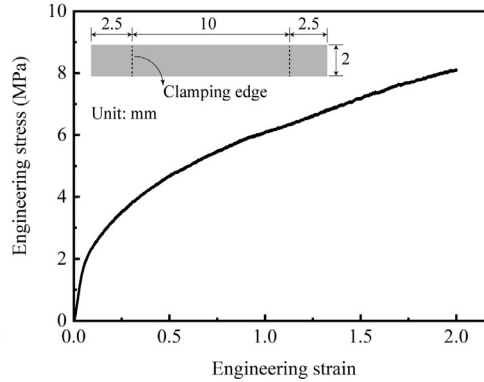
It followed that the nominal densification strain $\varepsilon_D = 0.54$, as shown in Fig. 3a. The measured compressive response of the foam was
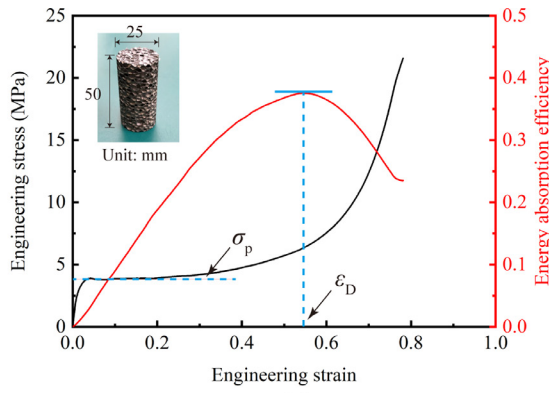
Fig. 3. (a) Measured compressive engineering stress versus engineering strain curve of aluminum foam at strain rate of $1 \times 10^{-3}\,\mathrm{s}^{-1}$, (b) measured tensile true stress versus true strain curve of AISI 304 stainless steel at strain rate of $3.3 \times 10^{-3}\,\mathrm{s}^{-1}$, and (c) uniaxial tensile curve of rubberized sealing tape at strain rate of $6.7 \times 10^{-3}\,\mathrm{s}^{-1}$.

employed to perform subsequent numerical simulations in order to explore systematically the deformation process of the proposed sandwich beam under foam projectile impact. In addition, uniaxial tensile test at a nominal strain rate of $3.3 \times 10^{-3}\,\mathrm{s}^{-1}$ was conducted on a MTS machine, in accordance with the ISO standard 6892–1:2009, to determine the mechanical properties of annealed AISI 304 stainless steel. Standard dog-bone samples were cut from as-received AISI 304 plates and .subjected to the same brazing cycle used to manufacture the sandwich beams. Force and displacement profiles generated in the MTS machine were simultaneously recorded to generate the true stress-true strain curve as shown in Fig. 3b. Three tests were conducted on specimens having the same thickness. Generally speaking, the AISI 304 stainless steel may be regarded as an elastic, linearly hardening material, with density $\rho_s = 7800\,\mathrm{kg\,m}^{-3}$, Young's modulus $E_s = 200\,\mathrm{GPa}$, yield strength $\sigma_Y = 200\,\mathrm{MPa}$ and tangent modulus $E_t = 2\,\mathrm{GPa}$. In addition, uniaxial tensile test of the sealing tape was conducted at a nominal strain rate of $6.7 \times 10^{-3}\,\mathrm{s}^{-1}$ following the Standard Test Method for Tensile Properties of Thin Plastic Sheeting (ASTM D882-12). For consistency, only average results from three experimental tests were reported below, as shown in Fig. 3c.

2.3. Impact testing of foam projectile

Fig. 4 displayed the experimental set-up of impact tests, which consisted of a gas gun, laser gates, a high-speed camera, a laser displacement transducer, and a pair of fixtures. To propel a foam projectile through the barrel, nitrogen gas was supplied to the gas gun at a pressure prescribed in the pressure vessel. The gas gun had a barrel length of $l_g = 5\,\mathrm{mm}$ and an outer diameter of $d_g = 135\,\mathrm{mm}$. The fixture was used for clamping the specimen at the supporting edges. There were a total of six M10 bolts on the fixture, with three bolts located on each side.

Foam projectiles (length $l_0 = 85\,\mathrm{mm}$) electro-discharge machined from close-celled aluminum foam cylinders were used to centrally

impact the fully end-clamped sandwich beam over a central circular patch of diameter $d = 57\,\mathrm{mm}$. To prevent tumbling, the length-diameter ratio of the projectile should be within the range of $0.82 \sim 1.75$ [40,44]. Moreover, the loading region was slightly smaller than the beam width in order to avert the varying response of the corrugated core across its width direction [40]. The velocity of the projectile was measured at the exit of the barrel using laser gates, and a high-speed camera (I-SPEED 716, IX) was used to observe the structural evolution of the sandwich beam at the maximum frame rate and exposure time of 10^6 fps and 1 μs, respectively. After experiments, the sandwich beam was removed from the fixture and examined to measure the permanent deflection profiles of its face sheets and the compressive deformation of its corrugated core.

3. Experimental results

In this section, experimental results (e.g., structural evolution via high-speed photos, deformation/failure modes via final deformed profiles) were presented, compared and employed to analyze the effects of water filling on resisting local projectile impact. For both empty and water-filled sandwich beams with corrugated cores, Table 3 summarized the experimental results at selected values of impact impulse I_p. Note that, m_c and m_w represent the mass of the beam and the filled water, respectively; w_f and w_b are the permanent mid-span deflection of the front and back face sheets, respectively, and ε_c is the permanent mid-span core compression given by:

$$\varepsilon_c = \frac{w_f - w_b}{l_c \sin\theta + t_c} \tag{5}$$

3.1. Structural evolutions

Seven levels of impact impulses were applied to empty sandwich beams (samples **EC-1~7** in Table 3) by varying the impact velocity of
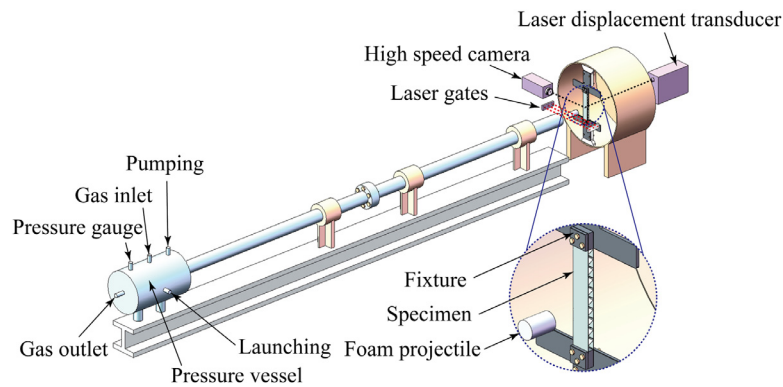
Fig. 4. Schematic of overall impact testing setup.

the foam projectile. The measured dynamic responses were analyzed, as below. Under a local projectile impact, the structural response of a clamped sandwich beam may be classified into three stages, as [45,46]: (i) in the first stage, as the corrugated core is fold under the projectile impact, the velocity of the front face sheet decelerates while the back face sheet accelerates, which ends when the velocities of the two face sheets approach equal; (ii) in the second stage, the front and back face sheets move together until the sandwich beam comes to rest at the point of maximum mid-span deflection, causing the overall deformation of combined plastic bending and longitudinal stretching; (iii) in the third stage, elastic oscillation occurs, with the mid-span deflection of front and back face sheets fluctuating within a small scale and eventually approaching stable values. Similar dynamic response behaviors were observed in the present experiments.

Figs. 5–7 presented the evolution histories of deformation and failure in selected empty sandwich beams (i.e., **EC-3, 5** and **7**) with I_p = 4.3, 6.2, 9.0 kPa s, respectively. The time labeled on the high-speed photo sequences was measured from the instant of foam projectile impact, and the marked red line was used to assist differentiating the mid-span deflection of the back face sheet. As could be seen from Fig. 5**a**, when the cylindrical foam projectile arrived at the front face sheet, the corrugated core within the loading patch started to be compressed in a high-order buckling mode, followed by progressive collapse concentrated near the front face. Two pairs of plastic hinges initiated at the edge of the circular impact region, and then travelled towards beam supports and mid-span, respectively. Once the plastic hinges reached both ends and the midpoint, the large shear stress between the face sheets and the corrugated core might lead to interfacial failure of the brazing joints only if the impact impulse reached a threshold, as shown in Fig. 6**a** and Fig. 7**a**.

Three different levels of impact impulses were also applied to water-filled sandwich beams (i.e., **WFC-1 ~ 3**), and their structural response were compared with those of the empty sandwich beams (i.e., **EC-3, 5** and **7**). Note that, a few white stripes appearing in the sealing tape were

not air bubbles but caused by light reflection of the transparent sealing tape. However, due to the present manual sealing process, the sandwich beams could not be fully filled with water so that small air bubbles were likely generated. Similarly, once the projectile impacted the front face, the corrugated core started to buckle, progressively fold and even reach densification. However, as the filled water was constrained in a limited space and was incompressible, the fast moving front face drove the bulk water to interact violently with the immersed corrugation members, the sealing tape and the back face. For instance, with beam **WFC-1**, numerous small air bubbles firstly occurred and grew in the central regime immediately below the impact, and then appeared near the clamped ends, as shown in Fig. 5**b**. With further increase of the impact impulse, the bulk water was enhanced in the degree of fragmentation, enabling the jet to escape via cracking the sealing tape. As shown in Fig. 6**b**, the crack, once initiated in the sealing tape, propagated from the central region to the supports along the longitudinal direction of the beam. As marked by red arrows in Fig. 6**b**, the cracking direction of the sealing tape could be inferred from the observed motion of the filled water, which was further confirmed by the final tearing crack morphology of the sealing tape as shown in Fig. 10. As for beam **WFC-3**, although a severe fracture of the sealing tape was observed in Fig. 10, cracking of the sealing tape along the same direction also occurred as marked by the red arrows in Fig. 7**b**. For beam **WFC-3**, the sealing tape started to fail at t = 0.1 ms under foam projectile impact. By contrast, the sealing tape of beam **WFC-2** failed at t = 0.4 ms as the core underwent a larger period of compression. Besides, for **WFC-3**, the onset of tape rupture occurred firstly at the center of the impact site, while that of **WFC-2** started to fail near the edge of the impact site. This indicated that, as the impact impulse was increased, interaction between the bulk water and the tape grew stronger and the tape began to rupture earlier during impact. Later, these experimental observations were further analyzed and discussed using numerical simulations.

Table 3
Experimental results for both empty and water-filled sandwich beams with corrugated cores.

| Specimen	Structural information			Projectile information			Mid-span deflection		
	Filling strategy	m_c (g)	m_w (g)	m_p (g)	v_p (m s^{-1})	I_p (kPa s)	w_f (mm)	w_b (mm)	ε_c
EC-1	Empty	1257	/	79.4	93	2.9	25	21	0.22
EC-2	Empty	1275.6	/	77.8	119	3.6	31	27	0.22
EC-3	Empty	1261.4	/	79.4	140	4.3	37	31	0.34
EC-4	Empty	1264.2	/	80	173	5.4	42	33	0.51
EC-5	Empty	1256.2	/	81.4	194	6.2	46	36	0.56
EC-6	Empty	1256.6	/	78.6	245	7.6	50	38	0.67
EC-7	Empty	1272	/	82.4	278	9.0	55	43	0.67
WFC-1	Water	1233.2	325.8	79.2	137	4.3	28	24	0.22
WFC-2	Water	1229.8	333.2	81	198	6.2	37	31	0.34
WFC-3	Water	1234.8	333.4	82.2	277	9.0	49	39	0.56
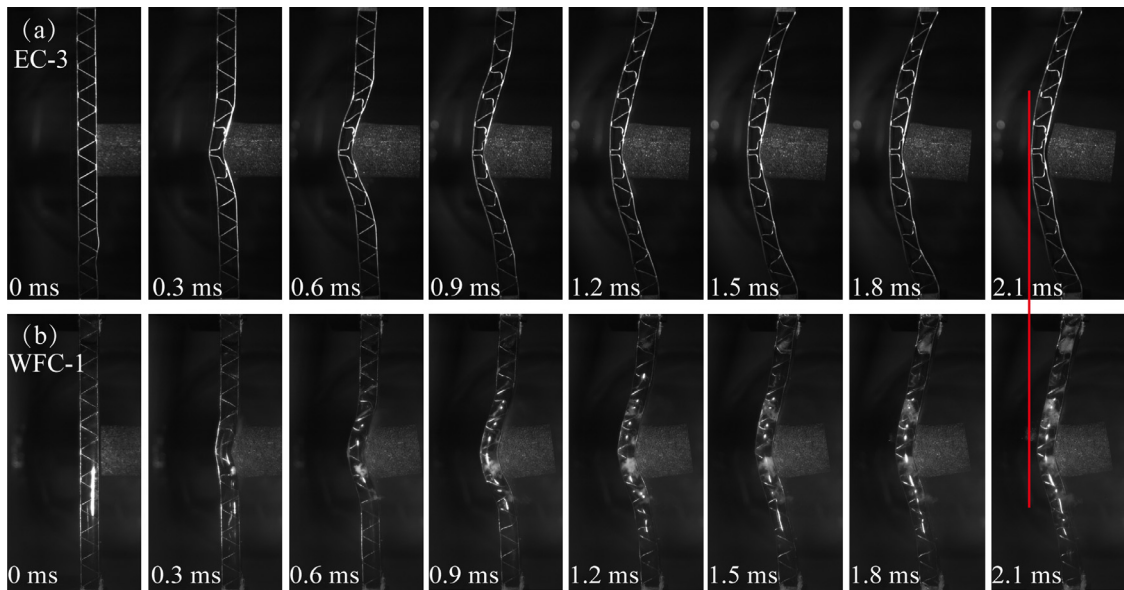
Fig. 5. Structural evolution of (a) empty corrugated sandwich (**EC-3**) and (b) water-filled corrugated sandwich (**WFC-1**) under a relatively low impact impulse of I_p = 4.3 kPa s. Inter-frame time of high-speed photo sequences was 0.05 ms and the time marked in each photo was measured from the instant of impact.

3.2. Deformation/failure modes

Fig. 9 displayed a montage of the final deformed profiles of empty sandwich beams. Concerning fully-clamped beams subjected to uniform blast loading, three distinctive failure modes had been classified, as [47]: large inelastic deformation, tensile tearing at the boundary, and shearing at the supports. In the current study, the sandwich beams subjected to foam projectile impacting exhibited quite similar deformation/failure modes (Fig. 9). For the front/back face sheets, no failure in the form of tensile tearing or shear failure across the beam section or around the clamped ends was observed [47], and only global inelastic deformation consisting of plastic bending and stretching was produced. Further, the corrugated core buckled progressively and folded up to full densification at beam center, while the extent to which the core was compressed decreased from the center to near both ends due to significant shear deformation in the clamped region. When

the impact impulse was relatively low (e.g., beams **EC-1~2**), plastic buckling was observed to be the main deformation mode, and the buckling direction was opposite to the direction of initial geometric imperfection, attributed to the inertia effect [48]. For relatively high impulses (e.g., beams **EC-6~7**), two regions of the deformed core (fully folded and partially folded region) were distinguished. In beam **EC-5**, a typical collapse mode called "stubbing" occurred in the central region of the beam, similar to that reported in McShane et al. [49]. Transverse bending of the buckled corrugation members within the impact region (ellipses in red solid line) enabled them to contact with the moving front face. This implied that, when the corrugation members folded against the moving front face, the interference of these members with the front face interrupted the full development of an axial buckle wave [18]. In addition, two dominating wavelets were clearly observed along these deformed corrugation members. Depending upon the magnitude of the impact impulse, local interfacial failure of brazing joints was
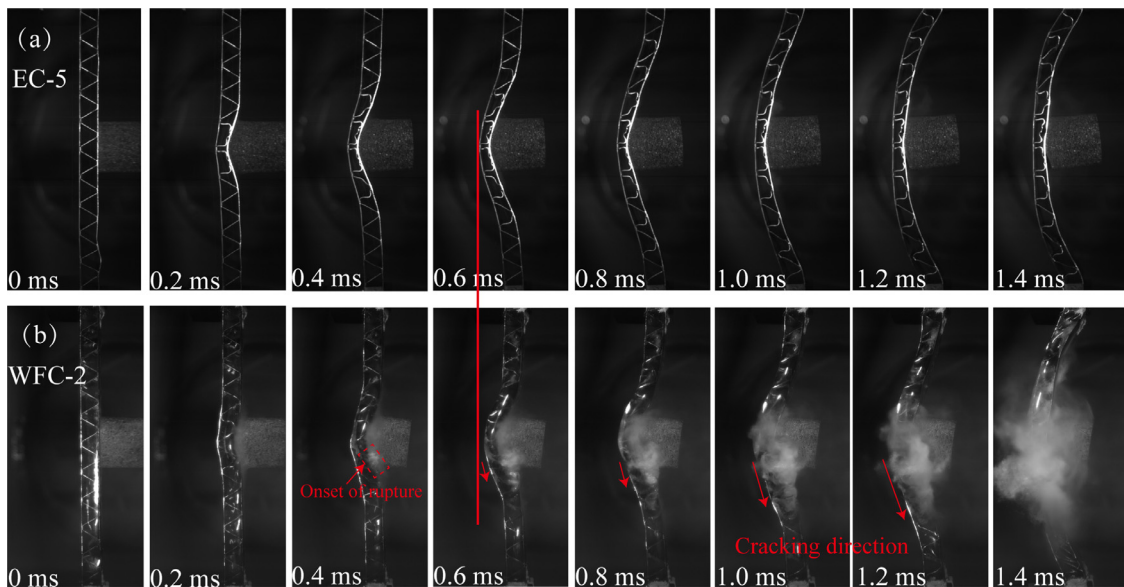

Fig. 6. Structural evolution of (a) empty corrugated sandwich (**EC-5**) and (b) water-filled corrugated sandwich (**WFC-2**) under a moderate impact impulse of I_p = 6.2 kPa s.
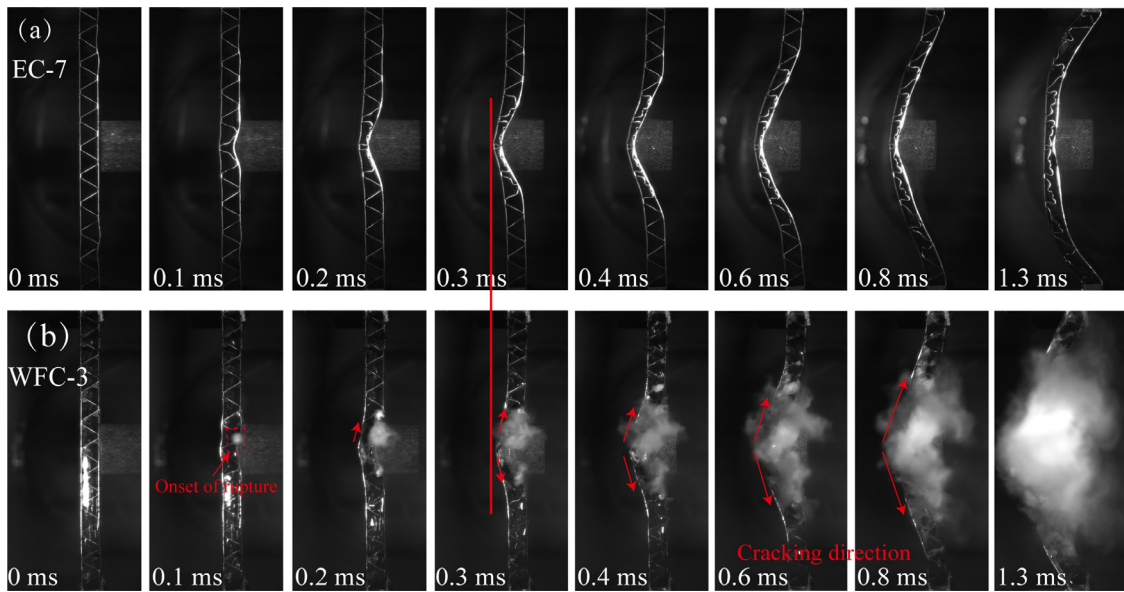
Fig. 7. Structural evolution of (a) empty corrugated sandwich (**EC-7**) and (b) water-filled corrugated sandwich (**WFC-3**) under a high impact impulse of I_p = 9.0 kPa s.
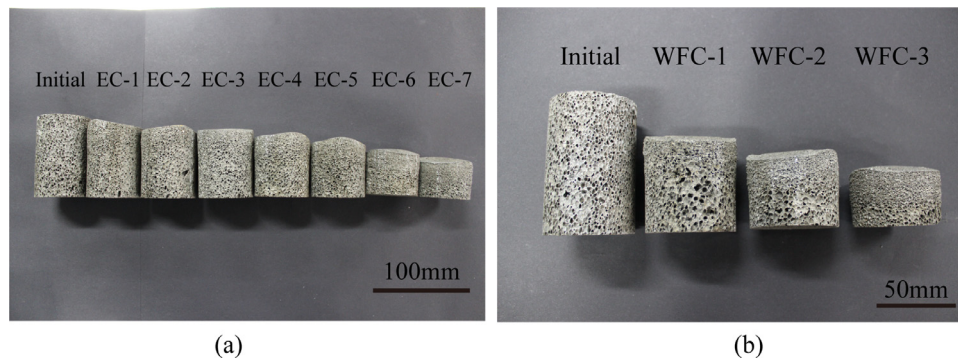

Fig. 8. Final profiles of dynamically loaded foam projectiles for (a) empty corrugated beams and (b) water-filled corrugated beams. For reference, undeformed (as-received) foam projectiles were also displayed.

observed firstly near the clamping regions (as depicted in beam **EC-4**), and then extended into the impacting regime (as seen in beam **EC-5**). Further increasing the impulse enabled the brazing fracture to propagate from the outer area to the center, eventually achieving global debonding. At this point, the front face was fully detached from the core as shown in beam **EC-7**. For empty sandwich beams, Fig. 8a compared the deformed profiles of foam projectiles with the as-received one. It was seen that the compression of foam projectile increased as the impacting velocity was increased, as expected.

A montage of the final deformed profiles of water-filled sandwich beams was displayed in Fig. 10, from which ta variety of deformation/failure modes for each constituent (front face, back face, corrugated core, sealing tape, *etc.*) were observed and compared with those shown in Fig. 9. For both face sheets, large inelastic deformation remained the dominating deformation mode, but significant difference in core deformation existed. For beam **WFC-1**, the resistances of its corrugation members against plastic buckling and progressive fold were enhanced, causing lesser core compression compared to beam **EC-3**. Similar phenomena were observed in beams **WFC-2** and **WFC-3**. Two likely aspects were considered for this enhancement: (i) the sealed water provided a lateral supporting force to the corrugation member against deformation and buckling as a result of its incompressibility, and (ii) the presence of incompressible filled water in the limited core space made it more difficult for corrugation members to deform and buckle relative to those in empty beams. In the present experimental tests, the sealing tape

constrained the motion of the bulk water, and seriously affected the interaction between the liquid and the beam members. Three typical deformation/failure modes could be observed and defined, as follows: (i) bulged deformation (**WFC-1**), (ii) local tearing (**WFC-2**), and (iii) overall fracture (**WFC-3**). As the impacting velocity was increased, the pressure transferred to the tape might also increase. Although disastrous failure occurred in the sealing tape, the bonding between the face sheets and the tape remained approximately intact, as depicted in Fig. 10. In terms of interfacial failure, depending upon the magnitude of the impact impulse, local interfacial failure of the brazing joints was observed, firstly near the clamping regions and then extended to the impacting location. For water-filled sandwich beams, Fig. 8**b** compared the deformed profiles of foam projectiles with the as-received one.

3.3. Quantitative results

Fig. 11 presented the measured half profiles of face sheet deflections for representative empty and water-filled corrugated sandwich beams. Filling water into the corrugated core significantly reduced the deflection profile along the direction of beam length. In the cases considered in the current study, the whole mass of the end-clamped corrugated sandwich beam was increased by around 26% as a result of water filling. However, the benefit of water filling on resisting mid-span deflections was dependent upon the foam impact impulse. As the impact impulse was increased, the mid-span deflection of the back face was
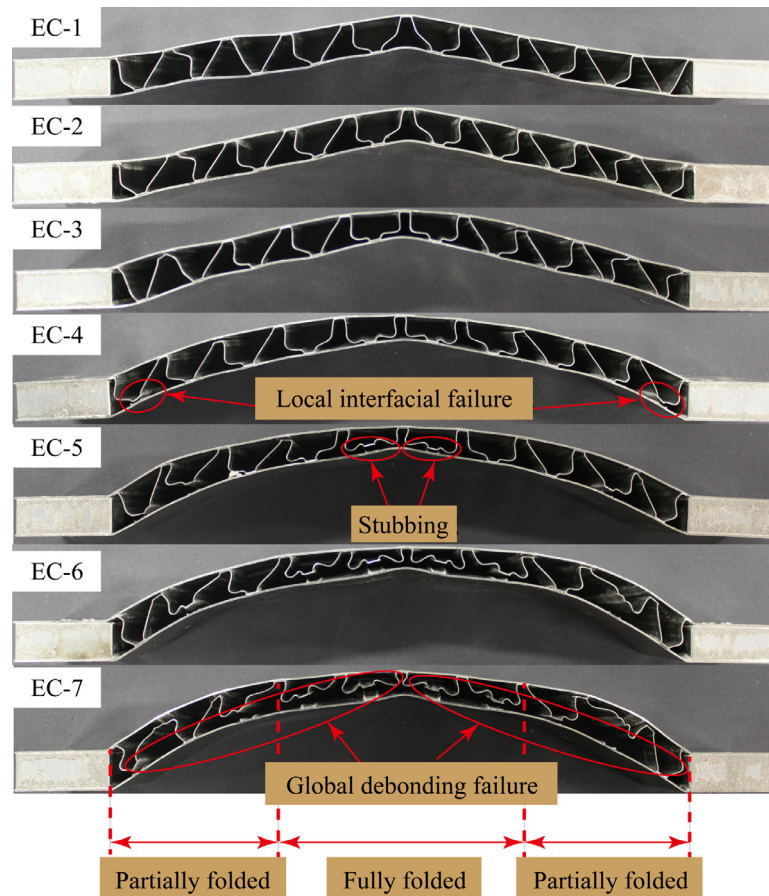
Fig. 9. Final profiles of dynamically loaded empty corrugated sandwich beams at selected values of foam projectile momentum, with typical deformation/failure modes highlighted.

reduced by 22.6%, 13.9% and 9.3%, respectively, while that of the front face by 24.3%, 19.6% and 10.9% (Fig. 11). Correspondingly, in terms of core compression, the maximum core compression in the central area was reduced by 35%, 39% and 16%, respectively. These results demonstrated that water filling was indeed effective in resisting structural deformation, as the confined bulk water provided a pressure to resist the deformation of face sheets and corrugation members owing to its inertia and manner of incompressibility. It should be mentioned however that, although further increasing the impact impulse enabled a higher pressure to support individual components of the sandwich beam, the pressure also led to earlier onset of failure in rubberized sealing tape, as observed in Fig. 6b and Fig. 7b. Following the rupture of sealing tape, water pressure was rapidly released, with fragmentation and flow of the filled water, and hence the interaction between the filling water and the sandwich components became much weaker. Similar mechanisms were discussed concerning the impact response of water-filled tubes [32–34].

4. Numerical predictions

The commercially available finite element (FE) program ANSYS v15.0 was utilized to model and mesh both empty and water-filled corrugated sandwich beams. The meshed models were subsequently transferred to the explicit integration version of FE code LS-DYNA R7 to conduct numerical simulations.

4.1. Numerical simulation model

4.1.1. Model description
Fig. 12a displayed the FE model of an empty corrugated sandwich

beam. Both the face sheets and the corrugated core were meshed using 4-node shell elements with Belytschko-Wong-Chiang formulation, while the foam projectile was meshed using 8-node solid elements. On both end of the sandwich beam, all degrees of freedom including displacements and rotations were restrained. The face sheets and the corrugated core were tied together using the tied surface-to-surface contact option, while automatic node-to-surface contact options were adopted for the projectile and face sheets. Fig. 12b showed the combined smoothed particle hydrodynamics-finite element (SPH-FE) model of a water-filled sandwich beam. To model the interaction between fluid and sandwich components, the bulk water was modelled using a mesh-free method (i.e., the SPH method), with a total of 199,800 nodes having an approximately equal distance of 1 mm. Automatic nodes-to-surface contact options were set for the filled water and the sandwich components, with additional option of soft constraint formulation employed. The most attractive feature of the SPH method is that it gets rid of the computation termination induced by likely large element distortion inherent in other FE models developed on the basis of Lagrangian formulation [50]. Thus, it is fit for expressing the interaction and flow of the bulk water observed in the tests. Compared with the Arbitrary Lagrange Euler (ALE) method, the SPH-FE model is relatively time-efficient and does not require the surrounding air to be represented in the model [51]. In addition, in the current study, the hourglass energy of the entire simulation model was controlled under 10% of the total energy, and the sliding energy was gradually eliminated by removing the initial penetration between smoothed particles and Lagrangian elements.

4.1.2. Material constitutive models
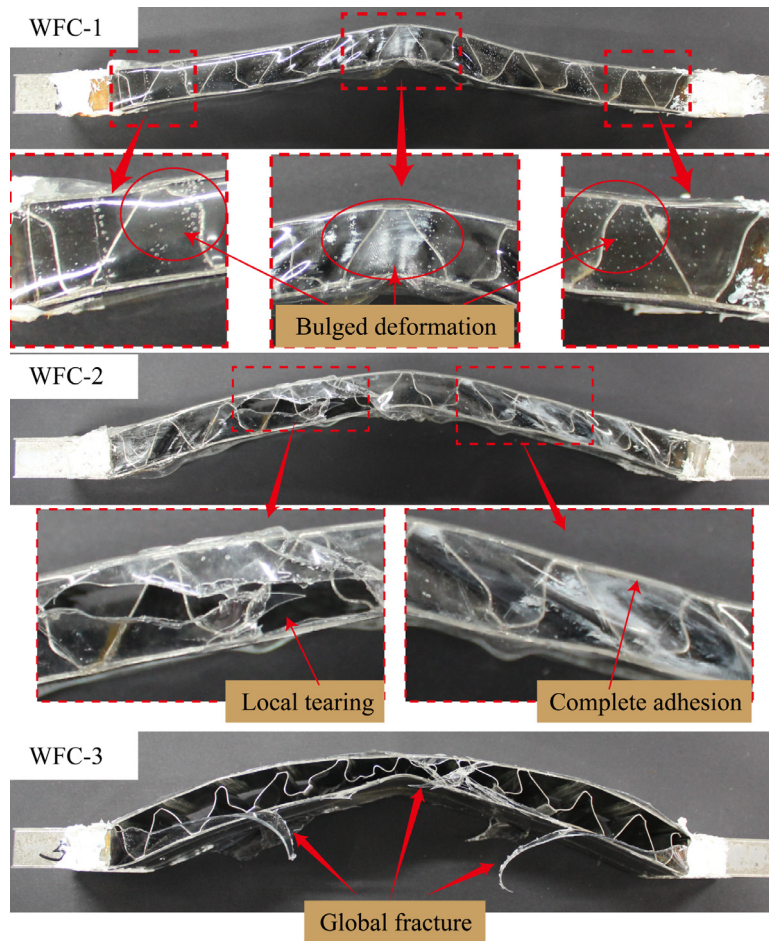The mechanical behavior of the parent material (AISI 304 stainless

Fig. 10. Final profiles of dynamically loaded, water-filled corrugated sandwich beams at selected values of foam projectile momentum, with typical deformation/failure modes highlighted.

steel) for corrugated sandwich beams was modelled using a plastic kinematic constitutive model (*MAT_PLASTIC_KINEMATIC), which can account for the strain rate effect via the Cowper-Symonds model, as [52]:

$$\frac{\sigma_{d}}{\sigma_{0}} = 1 + \left(\frac{\dot{\varepsilon}}{C}\right)^{\frac{1}{P}} \qquad (6)$$

where σ_{d} and σ_{0} were the dynamic and static yield stress, respectively, $\dot{\varepsilon}$ was the current strain rate, and (C, P) were the model parameters. The

mechanical properties of AISI 304 stainless steel, especially its rate sensitivity, were known to be sensitive to heat treatment histories. Lee et al. [53] found that the brazing procedure of all-metallic sandwich panels was similar to an annealing treatment for the base material, and the constitutive behavior of the base material was the same as that of annealed AISI 304 stainless steel. For the present corrugated sandwich beams, fitting existing experimental results of annealed AISI 304 stainless steel obtained under different strain rates [53,54] led to $C = 2623.57\,\mathrm{s}^{-1}$ and $P = 5.06$, as illustrated by the solid line and dots in Fig. 13. The close-celled aluminum foam projectile was simulated
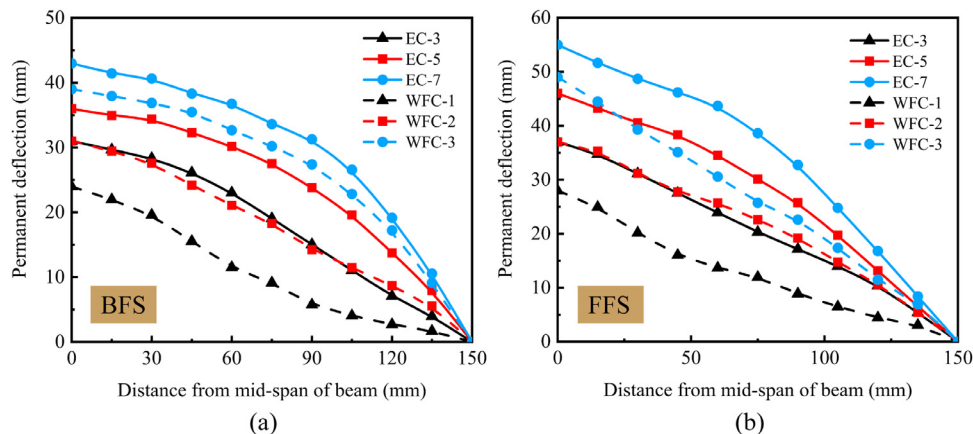

Fig. 11. Final measured profile of (a) back face sheet (BFS) and (b) front face sheet (FFS) plotted as a function of the distance from mid-span of beam.
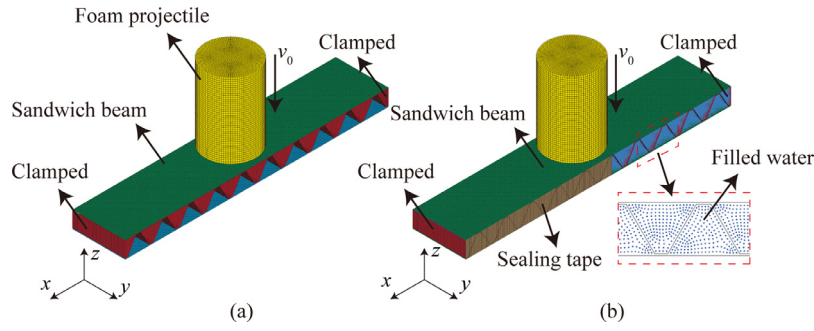
Fig. 12. (a) FE model of empty corrugated sandwich beam and (b) SPH-FE model of water-filled corrugated sandwich beam.
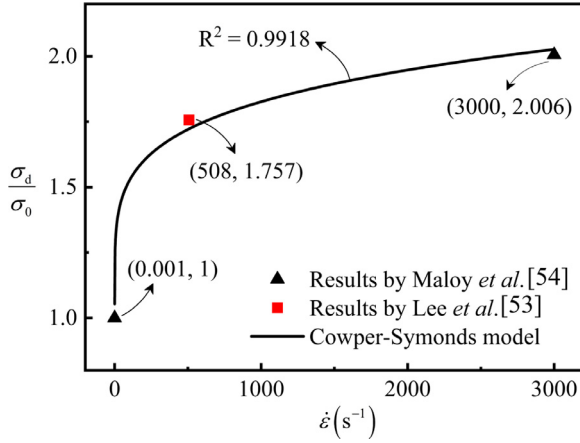

Fig. 13. Fitting results of yield strength ratio versus strain rate employed in Cowper-Symonds model.

Fig. 14. Fitting results of uniaxial tensile stress versus strain employed in the Mooney-Rivlin model for sealing tape.

using the foam constitutive model (*MAT_CRUSHABLE_FOAM), which accounted for strain rate sensitivity with a damping coefficient. In the present study, the damping coefficient was set as 0.1 [55].

For water-filled sandwich beams, the water was modelled using the model (*MAT_NULL), which allowed the equation of state (EOS) to be considered without computing deviatoric stresses. The corresponding Gruneisen EOS for pressure response was expressed as:

$$p = \frac{\rho_0 C^2 \mu \left[1 + \left(1 - \frac{\gamma_0}{2} \right) \mu - \frac{a}{2} \mu^2 \right]}{\left[1 - (S_1 - 1)\mu - S_2 \frac{\mu^2}{\mu+1} - S_3 \frac{\mu^3}{(\mu+1)^2} \right]} + (\gamma_0 + a\mu) E_I \tag{7}$$

where ρ_0, C, S_1, S_2, S_3, γ_0 and a were the input parameters, E_I was the internal energy per initial volume, and $\mu = \rho/\rho_0 - 1$. In the current study, the internal energy was neglected, $E_I = 0$. With rate sensitivity neglected, the sealing tape was simulated using a two-parameter rubber model (*MAT_MOONEY-RIVLIN_RUBBER). According to the Mooney-Rivlin theory [56,57], for an incompressible hyperelastic rubber-like material, its strain energy density function could be expressed as:

$$W = A(I_1 - 3) + B(I_2 - 3) \tag{8}$$

where A and B were two constant coefficients. I_1 and I_2 were the first and second invariant of the Cauchy-Green tensor, respectively:

$$I_1 = \lambda_1^2 + \lambda_2^2 + \lambda_3^2 \tag{9}$$

$$I_2 = \lambda_1^2 \lambda_2^2 + \lambda_2^2 \lambda_3^2 + \lambda_3^2 \lambda_1^2 \tag{10}$$

where λ_1, λ_2 and λ_3 were stretch ratios in the three principle directions of the Cauchy-Green tensor. In the case of uniaxial tension, $\lambda_1 = \lambda$, $\lambda_2 = \lambda_3 = 1/\lambda^{0.5}$ upon the assumption of volume incompressibility. Then, taking the derivative of the strain energy density with respect to the uniaxial stretch ratio λ led to the following stress–stretch relation:
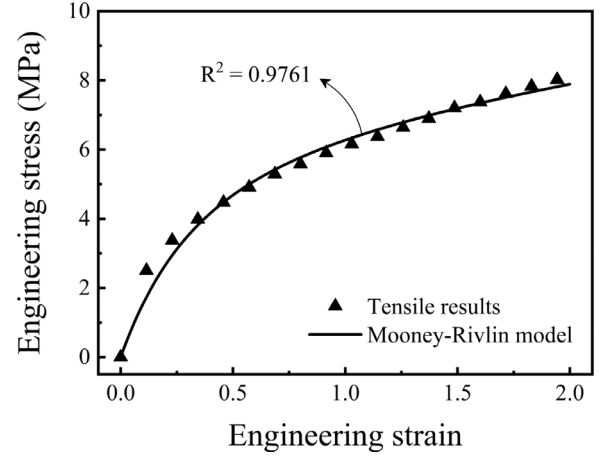
$$\sigma = \left(2A + \frac{2B}{\lambda} \right) \left(\lambda - \frac{1}{\lambda^2} \right) \tag{11}$$

$$\lambda = 1 + \varepsilon \tag{12}$$

Upon fitting the uniaxial tensile curve of Fig. 3c, the two undetermined parameters were obtained as $A = 0.5113$ MPa and $B = 2.563$ MPa (Fig. 14).

In addition, in the present FE simulations, the failure criterion of the sealing tape provided by the ADD_EROSION option (*MAT_ADD_EROSION) was employed, enabling the maximum principal strain criterion (MXEPS) to be selected. Through measurements (Fig. 3c), the engineering failure strain of the sealing tape was about 2.0, resulting in a true failure strain of about 1.0 under quasi-static uniaxial tensile loading. Similar to other rubberized materials [58], the failure behavior of the tape is sensitive to strain rate. However, obtaining experimentally an accurate relationship between the failure strain and strain rate over a wide range of strain rate is difficult and beyond the scope of the current research. Consequently, in subsequently FE simulations, the threshold failure strain was selected as 0.5 and 1.0 to preliminarily assess the failure behavior of sealing tape. Table 4 summarized the input parameters of the material models detailed above.

4.1.3. Mesh convergence

To obtain an optimal mesh size for FE simulations, mesh convergence test with different mesh sizes ($d_m = 0.5$, 0.75, 1.0, 1.25, 1.5 mm) was carried out. To this end, the empty sandwich beam was loaded under foam projectile impact with an initial velocity $v_0 = 150$ m/s; corresponding mid-span deflection-time curve of its back face sheet was displayed in Fig. 15. The permanent mid-span deflection was seen to converge as the mesh size was decreased, and the difference in simulation results obtained with mesh sizes $d_m = 0.5$, 0.75, 1.0 mm

Table 4
LS-DYNA input parameters of material constitutive models for numerical simulations.

| Component	Material	Material type and material property input data in LS-DYNA				
Sandwich beam	304 stainless steel	***MAT_PLASTIC_KINEMATIC (Material type 3)**				
		RO (kg m^{-3})	E (Pa)	PR	SIGY (Pa)	ETAN (Pa)	BETA
		7800	2E+11	0.3	2E+8	2E+9	0
		SRC (s^{-1})	SRP				
		2623.57	5.06				
Projectile	Aluminum foam	***MAT_CRUSHABLE_FOAM (Material type 63)**				
		RO (kg m^{-3})	E (Pa)	PR	LCID	TSC	DAMP
		378.3	1E+9	0	Fig. 2a	7.1E-3	0.1
Filling material	Water	***MAT_NULL (Material type 9)**				
		RO (kg m^{-3})	PC (Pa)	MU (Pa s)			
		1000	−10	0.89E-3			
		*EOS_GRUNEISEN					
		C (m s^{-1})	GAMMA	S1	S2	S3	
		1480	0.5	2.56	1.986	1.2268	
Sealing tape	Flex Seal®	***MAT_MOONEY-RIVLIN_RUBBER (Material type 27)**				
		RO (kg m^{-3})	PR	A (Pa)	B (Pa)		
		1143	0.495	0.5113E+6	2.563E+6		
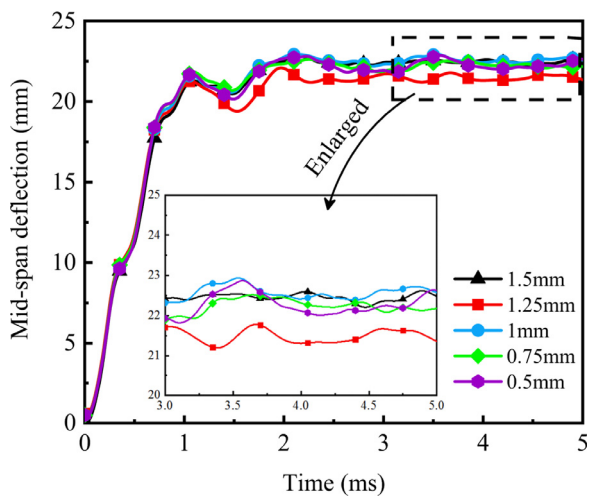
Fig. 15. Mesh convergence analysis: mid-span deflection versus time curves of back face sheet (BFS) simulated using five different mesh sizes.

was not obvious. Thus, for balanced computational cost and numerical accuracy, the mesh size $d_m = 1.0$ mm was adopted.

4.2. Validation and analysis

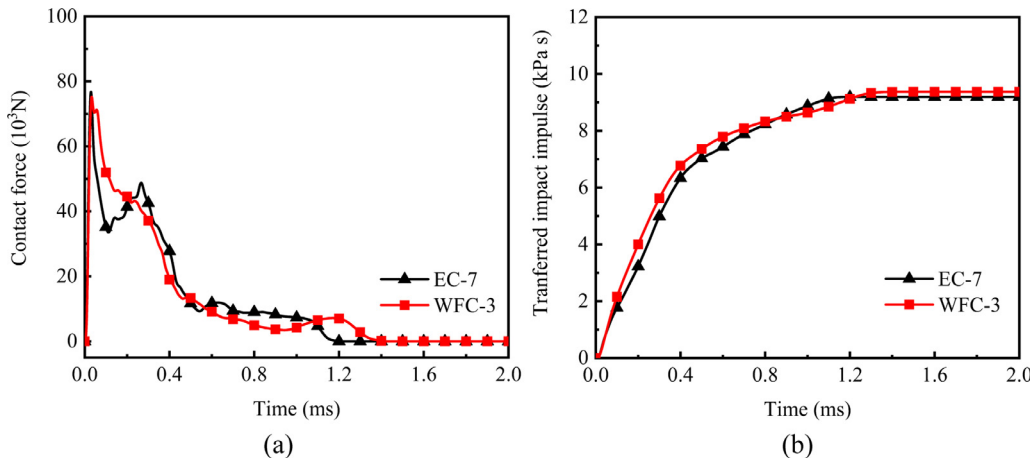Fig. 16a displayed typical evolution curves of the contact force between foam projectile and front face for $I_p = 9.0$ kPa s, corresponding to empty beam **EC-7** and water-filled beam **WFC-3**. When struck by foam projectile, pressure on the front face sharply increased from zero to a peak, then decreased rapidly and eventually dropped to zero. Notably, the empty and water-filled sandwich beams exhibited approximately the same contact force histories. The impact impulse per unit area transferred by the foam projectile was calculated by integrating the contact force with duration; the results were presented in Fig. 16b. The transferred impulse sharply increased during the early stage of impact and then gradually approached towards a stable value, which was approximately the same as the initial momentum of the foam projectile.

Subsequently, energy conservation of the whole system was investigated to ensure the correctness of the present numerical simulation results. For both **EC-7** and **WFC-3**, the predicted energy evolution histories were presented in Fig. 17. It was seen that, at any time after the impact, the sum of kinetic energy, internal energy and hourglass energy was equal to the total energy of the whole system. The hourglass energy just accounted for within 10% of the total energy, while the sliding energy was much less than 10% of the internal energy. Further, the kinetic energy of the foam projectile was almost completely transferred to the internal and kinetic energy of the whole system, in consistency with the experimental results. Overall, the numerical simulations reached a good balance of energy.

Permanent deflections were estimated by averaging the displacement over several cycles of elastic oscillation (from trough to peak) immediately after the initial maximum displacement, as shown in Fig. 18. For empty corrugated sandwich beams, the numerically simulated permanent deflections of the back and front face sheets were
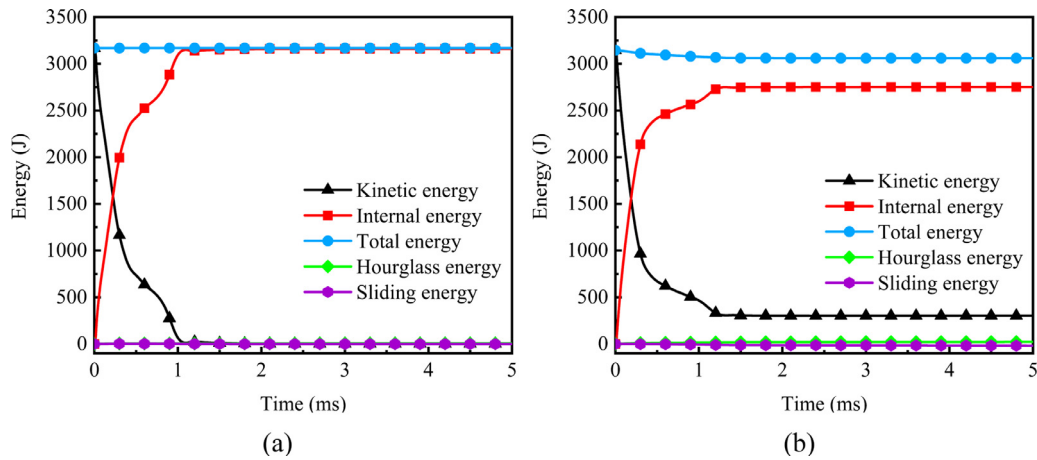

(a)

(b)

Fig. 16. (a) Representative contact force history curves between front face sheet (FFS) and foam projectile and (b) corresponding history curves of transferred impact impulse, for empty sandwich beam **EC-7** and water-filled sandwich beam **WFC-3**. The maximum principal strain at failure of the rubberized sealing tape was set as 0.5.

Fig. 17. Numerically predicted energy history of the whole system for (a) empty sandwich beam **EC-7** and (b) water-filled sandwich beam **WFC-3**, loaded by a projectile impact impulse of I_p = 9.0 kPa s. The maximum principal strain at failure of the rubberized sealing tape was set as 0.5.
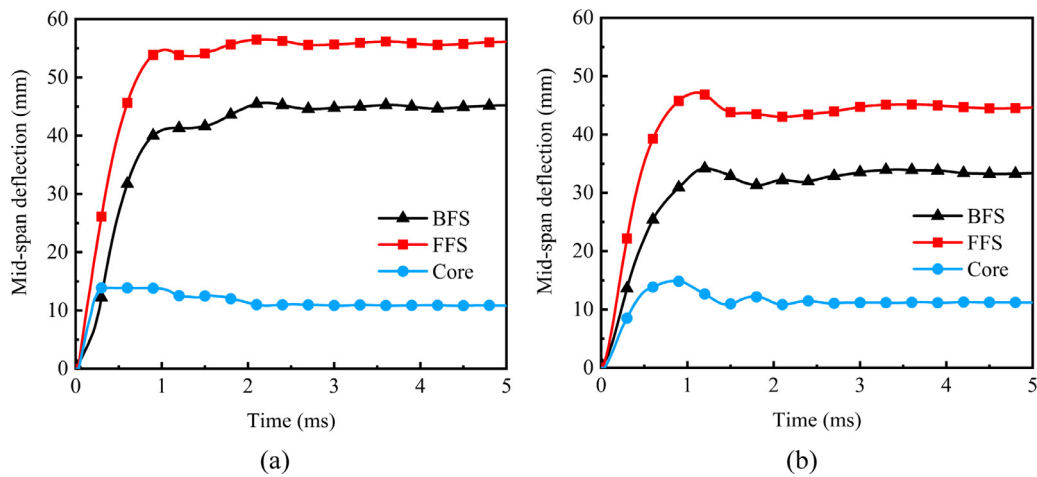

Fig. 18. Numerical predicted mid-span deflection versus time histories for (a) **EC-7** and (b) **WFC-3** loaded by a projectile impact impulse of I_p = 9.0 kPa s, with the maximum principal strain at failure of the sealing tape set as 0.5.
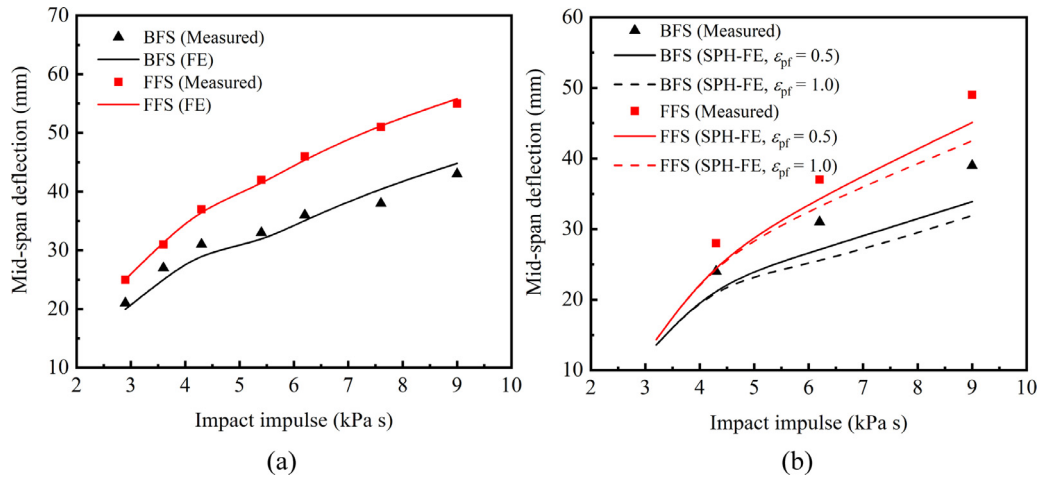

Fig. 19. Comparisons of experimental measurement results and numerical predictions on permanent mid-span deflections of BFS and FFS for (a) empty corrugated beams and (b) water-filled beams.

presented in Fig. 19**a,** together with the corresponding measured values. Good agreement between the measured results and FE predictions was achieved. On the other hand, in view of experimental observation, the SPH-FE model of water-filled beams should take the failure of sealing tape into consideration. Thus, a simple criterion of maximum

principal strain at failure ε_{pf} was selected to signify the dynamic rupture of the sealing tape. Fig. 19**b** compared experimental measurement results with numerical predictions for water-filled sandwich beams, with the threshold failure strain set as 0.5 and 1.0, respectively. The predicted deflections increased as ε_{pf} was decreased, implying that the
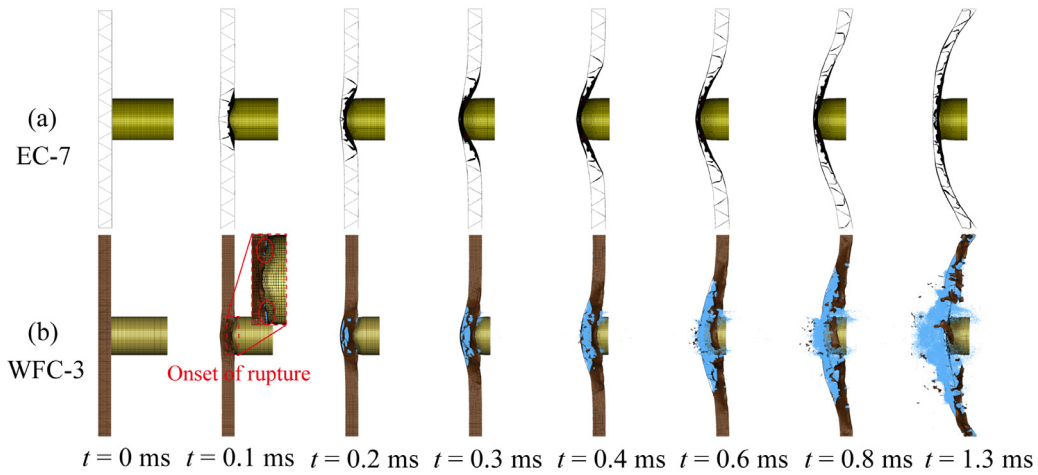
Fig. 20. Numerically predicted evolution of deformation in (a) **EC-7** (empty) and (b) **WFC-3** (water-filled; maximum principal strain at failure of sealing tape set as 0.5). Red circles represented the position where onset of rupture occurred in sealing tape.
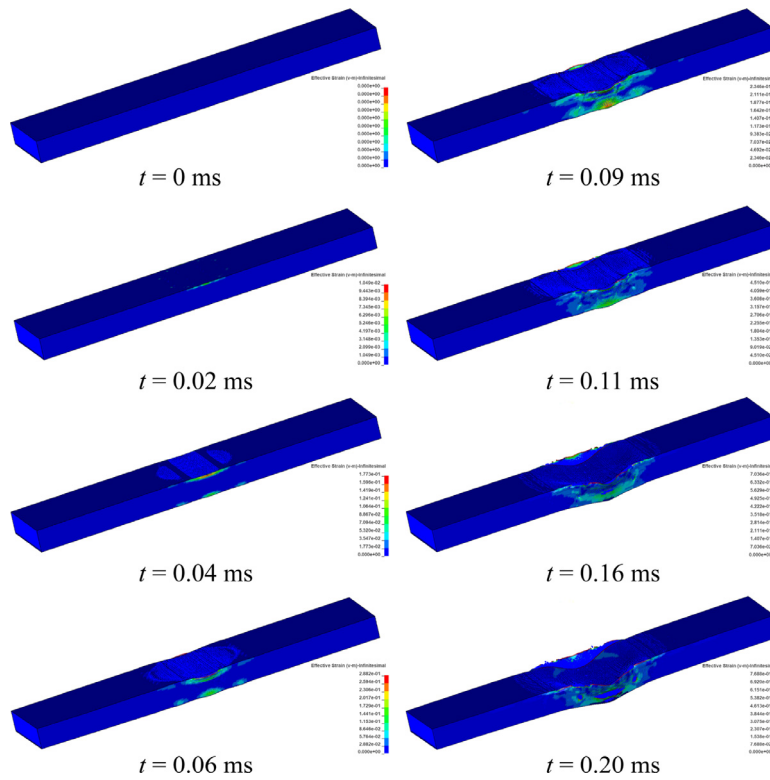

Fig. 21. Numerically simulated evolution of effective strain in water-filled **WFC-3** , with the maximum principal strain at failure of sealing tape set as 0.5.

earlier onset of rupture initiated in the sealing tape significantly affected the interaction between fluid and sandwich components. To a reasonable approximation, the predictions were consistent with experimental observations. However, discrepancies between predictions and measurements did exist (Fig. 19b), which was mainly attributed to: (i) the constraints of fixture applied on the beams were not completely representative of the clamped boundary condition assumed in FE simulations; (ii) debonding between face sheets and corrugated core was not considered in FE simulations; (iii) strengthening of rubberized sealing tape induced by strain rate sensitivity was not considered; (iv) fabrication defects and added mass of braze alloy were not explicitly accounted for in the numerical model.

In Fig. 20a~b, progressive evolution of deformation in empty and water-filled sandwich beams (**EC-7** and **WFC-3)** was separately presented for I_p = 9.0 kPa s. For the latter, the maximum principal strain at

failure of the rubberized sealing tape was set as 0.5. The FE simulation results were seen to in reasonable agreement with those experimentally observed in Fig. 7, including the large degree of core compression beneath foam projectile and the large shear deformation of core near the supported ends of each beam. Note that, although sophisticated simulation on the propagation process of the crack initiated in the sealing tape was not considered in the present FE simulations, the onset of tape failure could be approximately predicted, as shown in Fig. 20b. Fig. 21 displayed the predicted evolution of effective strain in **WFC-3**. High effective strain region was seen to first appear in the tape (under the impact site), then expand to the bottom through beam thickness direction, and finally propagate along beam length direction. Therefore, the onset of tape rupture was more likely to occur close to the impact site, consistent with experimental observation (Fig. 7b). The effects of sealing tape material properties on beam deformation and failure were
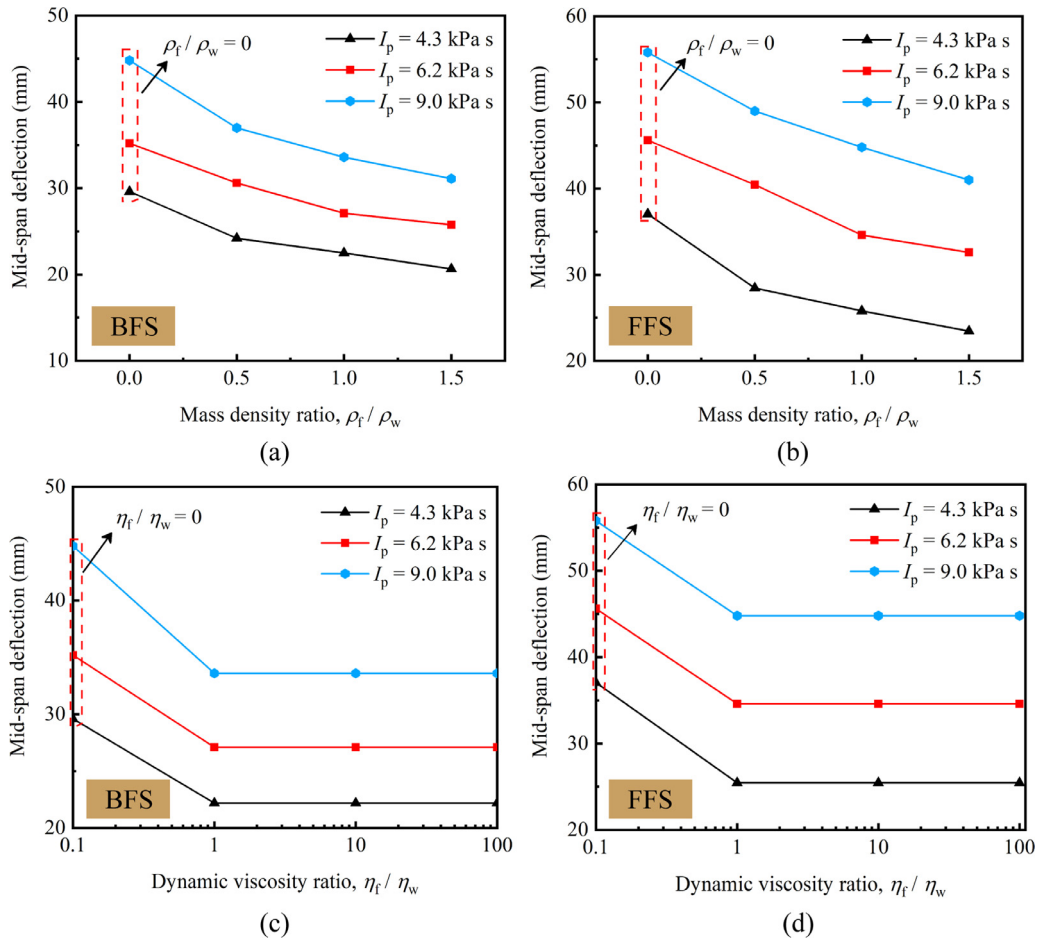
Fig. 22. Effect of fluid mass density on permanent mid-span deflection of (a) BFS and (b) FFS, and effect of fluid dynamic viscosity on permanent mid-span deflection of (c) BFS and (d) FFS, with maximum principal strain at failure of rubberized tape set as 0.5.
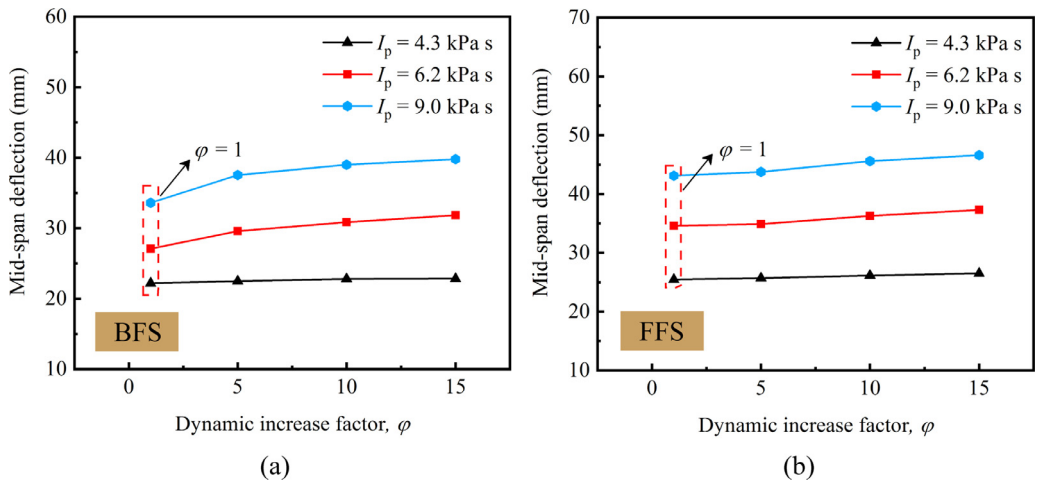

Fig. 23. Effects of dynamic increase factor φ on permanent mid-span deflection of (a) BFS and (b) FFS, with maximum principal strain at failure of rubberized tape fixed at 0.5.

further analyzed below with FE simulations.

4.3. Discussions

Thus far, it had been demonstrated, both experimentally and numerically, that the strategy of fluid filling could significantly enhance the impact resistance of end-clamped sandwich beams with corrugated cores. Compared with solid fillers (e.g., foam, sand, *etc.*), it is more convenient to fill bulk water into a sandwich structure without any complex retrofit. In the absence of serious blast/impact threat, the stored water in the sandwich core can be quickly released, and hence eliminates the concern of increased mass. For the cases considered in the present study, the strategy of fluid filling increased the whole mass of the sandwiches by approximately 26%, but the reduction in mid-span deflections of face sheets was as large as 24% (without any structural optimization). Under impact loading, the filled water provided strong

interaction between fluid and sandwich components owing to its inertia and incompressibility. Thus, the physical properties of fluid (density, dynamic viscosity, *etc.*) were expected to play important roles. Meanwhile, the solid-fluid interaction was directly associated with the mechanical properties (stiffness, strength, failure strain, *etc.*) of the sealing material, all of which were sensitive to strain rate.

4.3.1. Effects of filled fluid

Fig. 22 plotted the dependence of face sheet deflection on two essential physical properties of fluid: mass density ρ_f and dynamic viscosity η_f. The maximum principal strain at failure of the rubberized tape was set as 0.5. Two dimensionless parameters, ρ_f / ρ_w and η_f / η_w, were defined to express the mass density and dynamic viscosity ratio of the filled fluid and the bulk water (used in the present tests), with $\rho_f / \rho_w = 0$ or $\eta_f / \eta_w = 0$ representing empty sandwich beams. Three selected projectile impact impulses were dynamically loaded on corrugated sandwich beams, consistent with the impact tests. The mid-span deflections of face sheets significantly decreased with increasing ρ_f / ρ_w, but the rate at which the mid-span deflection decreased dropped as the fluid mass density was increased (Fig. 22**a** ~ **b**). Thus, the added inertia of the filled fluid played a vital role in resisting structural deformation. By contrast, the dynamic viscosity of the fluid had no obvious influence on the dynamic response of the sandwich beam: as shown in Fig. 22**c** ~ **d**, the mid-span deflections remained approximately constant when η_f / η_w was increased.

4.3.2. Effects of sealing material

Consider next how the basic mechanical properties (stiffness, strength and failure strain) of the sealing material affect the impact resistance of liquid-filled sandwich beams. In order to explain the current experimental results, the dependence of mid-span deflection on the failure strain of the sealing material was quantified, for it determined the duration of solid-fluid interaction. As shown in Fig. 19**b**, as the failure strain was increased, the onset of sealing rupture was initiated earlier and the mid-span deflections of both face sheets were significantly reduced. It was anticipated that rate sensitivity enabled the rubberized tape to have a smaller failure strain, thus causing the earlier onset of rupture close to the projectile impact area. Further, under a high strain rate loading, the tensile stiffness and strength of the sealing material should also be strengthened, similar to rubberized polymer materials [59].

Following Mohotti et al. [59], a strain-rate dependent term was added to Eq. (8) by introducing a dynamic increase factor φ. The modified stress-stretch relation of the Mooney-Rivlin model implemented in LS-DYNA R7 was thence rewritten as:

$$\sigma = \varphi(2c_{10} + \frac{2c_{01}}{\lambda})\left(\lambda - \frac{1}{\lambda^2}\right) \tag{13}$$

$$\varphi = 1 + \mu \ln \frac{\dot{\varepsilon}}{\dot{\varepsilon_0}} \tag{14}$$

where $\dot{\varepsilon_0}$ was the reference strain rate, $\dot{\varepsilon}$ was the current strain rate, and μ was the strain rate parameter. Adjusting the value of φ enabled investigating the effects of rate-induced strengthening of the sealing material, as illustrated in Fig. 23 for beam **WFC-3**. The results showed that strengthening the sealing material only slightly affected impact resistance of the present liquid-filled sandwich beams, with the fixed failure strain of sealing material.

5. Concluding remarks

The main motivation of this investigation was to evaluate the effects of fluid filling on resisting structural deformation of end-clamped, all-metallic corrugated sandwich beams subjected to simulated foam projectile impact. A combined experimental and numerical approach was employed to quantify the benefits of fluid filling and explore the

underlying mechanisms, with main conclusions summarized as below.

(i) Water filling enhanced significantly the impact resistance of corrugated sandwich beams, due mainly to the strong interaction between water and sandwich components as a result of the inertia and incompressibility of water;

(ii) The filled water decreased the level of inelastic deformation of the face sheets along beam length, and improved the resistance of the corrugated core against plastic buckling and progressive folding;

(iii) The SPH-FE model of water-filled sandwich beams could simulate fluid-solid interaction and provide reasonable predictions of permanent structural deformation, core compression, and onset of failure in the sealing tape;

(iv) The benefit of fluid filling for enhanced impact resistance was correlated strongly with the mass density of the fluid and slightly with the rate-induced strengthening of the sealing material, but insensitive to the dynamic viscosity of the fluid.

CRediT authorship contribution statement

Xin Wang: Conceptualization, Methodology, Writing - original draft. **Run-Pei Yu:** Investigation, Data curation. **Qian-Cheng Zhang:** Formal analysis, Writing - review & editing. **Lang Li:** Investigation. **Xue Li:** Software, Visualization. **Zhen-Yu Zhao:** Validation. **Bin Han:** Investigation. **Si-Yuan He:** Investigation, Resources. **Tian Jian Lu:** Supervision, Conceptualization, Funding acquisition.

Declaration of competing interest

The authors declare that they have no known competing financial interests or personal relationships that could have appeared to influence the work reported in this paper.

Acknowledgments

References

[1] Hutchinson JW, Xue Z. Metal sandwich plates optimized for pressure impulses. Int J Mech Sci 2005;47:545–69. https://doi.org/10.1016/j.ijmecsci.2004.10.012.

[2] Dharmasena KP, Wadley HNG, Williams K, Xue Z, Hutchinson JW. Response of metallic pyramidal lattice core sandwich panels to high intensity impulsive loading in air. Int J Impact Eng 2011;38:275–89. https://doi.org/10.1016/j.ijimpeng.2010.10.002.

[3] McShane GJ, Deshpande VS, Fleck NA. Underwater blast response of free-standing sandwich plates with metallic lattice cores. Int J Impact Eng 2010;37:1138–49. https://doi.org/10.1016/j.ijimpeng.2010.05.004.

[4] Rubino V, Deshpande VS, Fleck NA. The dynamic response of end-clamped sandwich beams with a Y-frame or corrugated core. Int J Impact Eng 2008;35:829–44. https://doi.org/10.1016/j.ijimpeng.2007.10.006.

[5] Paik JK. Innovative structural designs of tankers against ship collisions and grounding: a recent state-of-the-art review. Mar Technol SNAME News 2003;40:25–33.

[6] Goel A, Uth T, Wadley HNG, Deshpande VS. Effect of surface properties on momentum transfer to targets impacted by high-velocity sand slugs. Int J Impact Eng 2017;103:90–106. https://doi.org/10.1016/j.ijimpeng.2017.01.001.

[7] Rubino V, Deshpande VS, Fleck NA. The dynamic response of clamped rectangular Y-frame and corrugated core sandwich plates. Eur J Mech A/Solids 2009;28:14–24. https://doi.org/10.1016/j.euromechsol.2008.06.001.

[8] Han B, Zhang ZJ, Zhang QC, Zhang Q, Lu TJ, Lu BH. Recent advances in hybrid lattice-cored sandwiches for enhanced multifunctional performance. Extrem Mech Lett 2017;10:58–69. https://doi.org/10.1016/j.eml.2016.11.009.

[9] Ha NS, Lu G. A review of recent research on bio-inspired structures and materials for

energy absorption applications. Elsevier Ltd 2019. https://doi.org/10.1016/j.compositesb.2019.107496.

[10] Yan LL, Yu B, Han B, Chen CQ, Zhang QC, Lu TJ. Compressive strength and energy absorption of sandwich panels with aluminum foam-filled corrugated cores. Compos Sci Technol 2013;86:142–8. https://doi.org/10.1016/j.compscitech.2013.07.011.

[11] Yan LL, Han B, Yu B, Chen CQ, Zhang QC, Lu TJ. Three-point bending of sandwich beams with aluminum foam-filled corrugated cores. Mater Des 2014;60:510–9. https://doi.org/10.1016/j.matdes.2014.04.014.

[12] Bin H, Bo Y, Yu X, Chang-Qing C, Qian-Cheng Z, Tian Jian L. Foam filling radically enhances transverse shear response of corrugated sandwich plates. Mater Des 2015;77:132–41. https://doi.org/10.1016/j.matdes.2015.03.050.

[13] Han B, Qin KK, Zhang QC, Zhang Q, Lu TJ, Lu BH. Free vibration and buckling of foam-filled composite corrugated sandwich plates under thermal loading. Compos Struct 2017;172:173–89. https://doi.org/10.1016/j.compstruct.2017.03.051.

[14] Yu B, Han B, Ni CY, Zhang QC, Chen CQ, Lu TJ. Dynamic crushing of all-metallic corrugated panels filled with close-celled aluminum foams. J Appl Mech 2015;82:011006https://doi.org/10.1115/1.4028995.

[15] Zhu F, Zhao L, Lu G, Wang Z. Deformation and failure of blast-loaded metallic sandwich panels-Experimental investigations. Int J Impact Eng 2008;35:937–51. https://doi.org/10.1016/j.ijimpeng.2007.11.003.

[16] Hou W, Zhu F, Lu G, Fang DN. Ballistic impact experiments of metallic sandwich panels with aluminium foam core. Int J Impact Eng 2010;37:1045–55. https://doi.org/10.1016/j.ijimpeng.2010.03.006.

[17] Shen J, Lu G, Wang Z, Zhao L. Experiments on curved sandwich panels under blast loading. Int J Impact Eng 2010;37:960–70. https://doi.org/10.1016/j.ijimpeng.2010.03.002.

[18] Zhang P, Cheng Y, Liu J, Li Y, Zhang C, Hou H, et al. Experimental study on the dynamic response of foam-filled corrugated core sandwich panels subjected to air blast loading. Compos Part B Eng 2016;105:67–81. https://doi.org/10.1016/j.compositesb.2016.08.038.

[19] Cheng Y, Liu M, Zhang P, Xiao W, Zhang C, Liu J, et al. The effects of foam filling on the dynamic response of metallic corrugated core sandwich panel under air blast loading – Experimental investigations. Int J Mech Sci 2018;145:378–88. https://doi.org/10.1016/j.ijmecsci.2018.07.030.

[20] Yazici M, Wright J, Bertin D, Shukla A. Experimental and numerical study of foam filled corrugated core steel sandwich structures subjected to blast loading. Compos Struct 2014;110:98–109. https://doi.org/10.1016/j.compstruct.2013.11.016.

[21] Yazici M, Wright J, Bertin D, Shukla A. Preferentially filled foam core corrugated steel sandwich structures for improved blast performance. J Appl Mech 2015;82:061005https://doi.org/10.1115/1.4030292.

[22] Liu J, Wang Z, Hui D. Blast resistance and parametric study of sandwich structure consisting of honeycomb core filled with circular metallic tubes. Compos Part B Eng 2018;145:261–9. https://doi.org/10.1016/j.compositesb.2018.03.005.

[23] Wang Z, Liu J. Mechanical performance of honeycomb filled with circular cfrp tubes. Compos Part B Eng 2018;135:232–41. https://doi.org/10.1016/j.compositesb.2017.09.048.

[24] Børvik T, Burbach A, Langberg H, Langseth M. On the ballistic and blast load response of a 20ft ISO container protected with aluminium panels filled with a local mass - Phase I: design of protective system. Eng Struct 2008;30:1621–31. https://doi.org/10.1016/j.engstruct.2007.10.011.

[25] Børvik T, Burbach A, Langberg H, Langseth M. On the ballistic and blast load response of a 20ft ISO container protected with aluminium panels filled with a local mass - Phase II: validation of protective system. Eng Struct 2008;30:1621–31. https://doi.org/10.1016/j.engstruct.2007.10.011.

[26] Kailasanath K., Tatem P.A., Mawhinney J. Blast mitigation using water-a status report. 2002.

[27] Venkataramana K, Singh RK, Deb A, Bhasin V, Vaze KK, Kushwaha HS. Blast protection of infrastructure with fluid filled cellular polymer foam. Procedia Eng 2017;173:547–54. https://doi.org/10.1016/B978-0-08-097086-8.12032-X.

[28] Schwer DA, Kailasanath K. Numerical simulations of the mitigation of unconfined explosions using water-mist. Proc Combust Inst 2007;31(II):2361–9. https://doi.org/10.1016/j.proci.2006.07.145.

[29] Shin YS, Lee M, Lam KY, Yeo KS. Modeling mitigation effects of watershield on shock waves. Shock Vib 1998;5:225–34. https://doi.org/10.1155/1998/782032.

[30] Wang Y, Zhou H. Numerical study of water tank under blast loading. Thin-Walled Struct 2015;90:42–8. https://doi.org/10.1016/j.tws.2015.01.012.

[31] Wang Y, Xiong MX. Analysis of axially restrained water storage tank under blast loading. Int J Impact Eng 2015;86:167–78. https://doi.org/10.1016/j.ijimpeng.2015.07.012.

[32] Xiaoqing M, Stronge WJ. Spherical missile impact and perforation of filled steel tubes. Int J Impact Eng 1985;3:1–16. https://doi.org/10.1016/0734-743X(85)90021-1.

[33] Nishida M, Tanaka K. Experimental study of perforation and cracking of water-filled aluminum tubes impacted by steel spheres. Int J Impact Eng 2006;32:2000–16. https://doi.org/10.1016/j.ijimpeng.2005.06.010.

[34] Lu GY, Zhang SY, Lei JP, Yang JL. Dynamic responses and damages of water-filled pre-pressurized metal tube impacted by mass. Int J Impact Eng 2007;34:1594–601. https://doi.org/10.1016/j.ijimpeng.2006.07.006.

[35] Varas D, López-Puente J, Zaera R. Experimental analysis of fluid-filled aluminium tubes subjected to high-velocity impact. Int J Impact Eng 2009;36:81–91. https://doi.org/10.1016/j.ijimpeng.2008.04.006.

[36] Radford DD, McShane GJ, Deshpande VS, Fleck NA. The response of clamped sandwich plates with metallic foam cores to simulated blast loading. Int J Solids Struct 2006;43:2243–59. https://doi.org/10.1016/j.ijsolstr.2005.07.006.

[37] Tagarielli VL, Deshpande VS, Fleck NA. The dynamic response of composite sandwich beams to transverse impact. Int J Solids Struct 2007;44:2442–57. https://doi.org/10.1016/j.ijsolstr.2006.07.015.

[38] Russell BP, Liu T, Fleck NA, Deshpande VS. The soft impact of composite sandwich beams with a square-honeycomb core. Int J Impact Eng 2012;48:65–81. https://doi.org/10.1016/j.ijimpeng.2011.04.007.

[39] Radford DD, Deshpande VS, Fleck NA. The use of metal foam projectiles to simulate shock loading on a structure. Int J Impact Eng 2005;31:1152–71. https://doi.org/10.1016/j.ijimpeng.2004.07.012.

[40] Rathbun HJ, Radford DD, Xue Z, He MY, Yang J, Deshpande V, et al. Performance of metallic honeycomb-core sandwich beams under shock loading. Int J Solids Struct 2006;43:1746–63. https://doi.org/10.1016/j.ijsolstr.2005.06.079.

[41] Wu X, Xiao K, Yin Q, Zhong F, Huang C. Experimental study on dynamic compressive behaviour of sandwich panel with shear thickening fluid filled pyramidal lattice truss core. Int J Mech Sci 2018;138–139:467–75. https://doi.org/10.1016/j.ijmecsci.2018.02.029.

[42] Andrews EW, Gioux G, Onck P, Gibson LJ. Size effects in ductile cellular solids. Part II: Experimental results. Int J Mech Sci 2001;43:701–13. https://doi.org/10.1016/S0020-7403(00)00043-6.

[43] Miltz J, Ramon OR. Energy absorption characteristics of polymeric foams used as cushioning materials. Polym Eng Sci 1990;30:129–33.

[44] Radford DD, Fleck NA, Deshpande VS. The response of clamped sandwich beams subjected to shock loading. Int J Impact Eng 2006;32:968–87. https://doi.org/10.1016/j.ijimpeng.2004.08.007.

[45] Fleck NA, Deshpande VS. The resistance of clamped sandwich beams to shock loading. J Appl Mech 2004;71:386. https://doi.org/10.1115/1.1629109.

[46] Qiu X, Deshpande VS, Fleck NA. Impulsive loading of clamped monolithic and sandwich beams over a central patch. J Mech Phys Solids 2005;53:1015–46. https://doi.org/10.1016/j.jmps.2004.12.004.

[47] Menkes SB, Opat HJ. Broken beams - Tearing and shear failures in explosively loaded clamped beams. Exp Mech 1973;13:480–6. https://doi.org/10.1007/BF02322734.

[48] Tilbrook MT, Radford DD, Deshpande VS, Fleck NA. Dynamic crushing of sandwich panels with prismatic lattice cores. Int J Solids Struct 2007;44:6101–23. https://doi.org/10.1016/j.ijsolstr.2007.02.015.

[49] McShane GJ, Pingle SM, Deshpande VS, Fleck NA. Dynamic buckling of an inclined strut. Int J Solids Struct 2012;49:2830–8. https://doi.org/10.1016/j.ijsolstr.2012.03.045.

[50] Liu MB. Liu GR. smoothed particle hydrodynamics (SPH): an overview and recent developments. Arch Comput Methods Eng 2010;17:25–76. https://doi.org/10.1007/s11831-010-9040-7.

[51] Olovsson L., Soulie Y.ALE and fluid-structure interaction capabilities in ls-dyn. vol. 414. 2000.

[52] LSTC. Keyword User ' S Manual VOLUME II Material Models. vol. II. 2007. https://doi.org/10.1016/j.chemosphere.2011.02.019.

[53] Lee S, Barthelat F, Hutchinson JW, Espinosa HD. Dynamic failure of metallic pyramidal truss core materials - Experiments and modeling. Int J Plast 2006;22:2118–45. https://doi.org/10.1016/j.ijplas.2006.02.006.

[54] Maloy SA, Gray GT, Cady CM, Rutherford RW, Hixson RS. The influence of explosive-driven "taylor-wave" shock prestraining on the structure/property behavior of 304 stainless steel. Metall Mater Trans A 2007;35:2617–24. https://doi.org/10.1007/s11661-004-0207-4.

[55] Jing L, Yang F, Zhao L. Perforation resistance of sandwich panels with layered gradient metallic foam cores. Compos Struct 2017;171:217–26. https://doi.org/10.1016/j.compstruct.2017.02.097.

[56] Mooney M. A theory of large elastic deformation. J Appl Phys 1940;11:582–92. https://doi.org/10.1063/1.1712836.

[57] Rivlin RS. Large elastic deformations of isotropic materials. IV. further developments of the general theory. Philos Trans R Soc A Math Phys Eng Sci 1948;241:379–97. https://doi.org/10.1098/rsta.1948.0024.

[58] Raghavan D, He J, Hunston D, Hoffman D. Strain rate dependence of fracture in a rubber-toughened epoxy system. J Adhes 2002;78:723–39. https://doi.org/10.1080/00218460213493.

[59] Mohotti D, Ali M, Ngo T, Lu J, Mendis P. Strain rate dependent constitutive model for predicting the material behaviour of polyurea under high strain rate tensile loading. Mater Des 2014;53:830–7. https://doi.org/10.1016/j.matdes.2013.07.020.